In situ Trace Element and Sulphur Isotope Analyses of Pyrite Constrain Timing of Mineralization and Sources of Sulphur in the Howard's Pass SEDEX Zn-Pb District, Yukon

M.G. Gadd and D. Layton-Matthews
Department of Geological Sciences and Geological Engineering, Queen's University, 36 Union Street, Kingston, ON, K7L 3N6
mggadd3@gmail.com

J.M. Peter
Geological Survey of Canada, 601 Booth Street, Ottawa, ON, K1A 0E8

S. Paradis
Geological Survey of Canada, 9860 West Saanich Road, Sidney, BC, V8L 4B2

Abstract

The Howard's Pass District, Yukon hosts twelve sedimentary exhalative (SEDEX) Zn-Pb deposits that contain approximately 393 Mt grading at 4.5% Zn and 1.5% Pb. Sulphide mineralization is hosted in carbonaceous and calcareous to siliceous mudstones. Pyrite is a minor but ubiquitous component. Detailed petrographic analysis reveals that pyrite has a complex and protracted growth history, with multiple generations of pyrite are preserved in single grains. Combined secondary ion mass spectrometry (SIMS) and laser ablation-inductively coupled plasma-mass spectrometry (LA-ICP-MS) analysis on paragenetically complex pyrite reveals that sulphur isotope and minor and trace element compositions mimic textural zonation. Sulphur isotope data imply that textural variability is genetically significant. In the SEDEX deposits, the earliest pyrite generation (i.e. framboids) have negative $\delta^{34}S$ values (mean -16.6‰), whereas later pyrite overgrowths and galena have positive $\delta^{34}S$ values (mean 29.1‰ and 22.4‰, respectively). The two sulphur isotope populations are interpreted to reflect contributions of bacterially reduced (negative) and thermochemically reduced (positive) seawater sulphate, and perhaps, of hydrothermally derived sulphate. LA-ICP-MS data provide information on the relative timing and cation content of depositional, hydrothermal and metamorphic fluids. These data also identify a suite of non-ore elements (Mn, As, Ag, Sb and Tl) associated with the Zn-Pb mineralizing fluids. These elements are spatially associated with both syngenetic to earliest diagenetic pyrite and with later diagenetic pyrite overgrowths. Together, these *in situ* analytical data suggest that SEDEX mineralization produced not only hydrothermal chemical sediments;

Recommended citation

Gadd, M.G., Layton-Matthews, D., Peter, J.M., and Paradis, S., 2015. In situ trace element and sulphur isotope analyses of pyrite constrain timing of mineralization and sources of sulphur in the Howard's Pass SEDEX Zn-Pb District, Yukon, *in* Paradis, S., ed., Targeted Geoscience Initiative 4: sediment-hosted Zn-Pb deposits: processes and implications for exploration; Geological Survey of Canada, Open File 7838, p. 58-74. doi:10.4095/296328

rather, dense metalliferous brine settled on, and percolated through, unconsolidated carbonaceous muds and precipitated metal sulphides in the subsurface.

Introduction

The Howard's Pass Zn-Pb District (HPD) of sedimentary exhalative (SEDEX) deposits comprises 12 Zn-Pb deposits that contain an estimated 393 Mt grading 4.5% Zn and 1.5% Pb (SCML, 2012). The HPD is located within the Selwyn Basin (Figure 1), a prolific metallogenic province that is primarily known for its world-class Zn-Pb (±Ag ±Ba) SEDEX deposits (Figure 1). SEDEX mineralization was discovered in the HPD in 1972 by following up regional stream-sediment geochemical anomalies. Exploration drilling during the 1970s and 2000s defined semi-continuous mineralization along a 38 km-long trend. The mineral deposits in the HPD remain undeveloped; however, an adit was driven in the XY deposit for test mining in 1981 (Goodfellow et al., 1983).

Mineralization in the HPD is composed mainly of massive and semi-massive sphalerite and galena hosted in carbonaceous mudstones; pyrite is a minor constituent (approximately 5.5 wt.%) of the mineralization. The trace element and stable isotope geochemistry of Howard's Pass pyrite has been the focus of previous studies (Morganti, 1979; Goodfellow et al., 1983; Goodfellow and Jonasson, 1984; Goodfellow, 1987) that used bulk analytical techniques on handpicked grains. Jonasson and Goodfellow (1986) identified several pyrite textures within the SEDEX deposits and their host rocks in the HPD, but separating very fine-grained intergrowths of sulphide minerals was not possible for bulk analysis.

Petrographic studies of pyrite with multi-generational growth textures have revealed changes in the morphology of pyrite in response to several stages of growth. In black shale successions, variations in pyrite textures have been interpreted to reflect spatial and temporal growth patterns (Berner, 1984; Raiswell and Berner, 1985; Large et al., 2014). During formation, pyrite is capable of sequestering numerous trace and minor elements (e.g. Ag, As, Au, Bi, Co, Cu, Mn, Mo, Ni, Pb, Sb, Se, Tl, Zn) and the contents of these reflect their availability during the various environments that existed during pyrite deposition (Large et al., 2009; Berner et al., 2013; Gregory et al., 2014). Texturally complex pyrite that experienced multiple generations of growth can record the ambient trace element budgets of the solutions from which it formed and can therefore be used as a proxy for the fluid history that may have involved one or more of hydrothermal, hydrogenous, diagenetic and metamorphic fluids. Pyrite that forms over a protracted period may also record variable sulphur isotope compositions (e.g. Eldridge et al., 1988; Eldridge et al., 1993; Ireland et al., 2004; Taylor, 2004). *In situ* sulphur isotope analyses (e.g. secondary ion mass spectrometry; SIMS) of different pyrite generations can therefore yield information about the mechanisms by which reduced sulphur was produced, as well as the sulphur budget of the ambient environment.

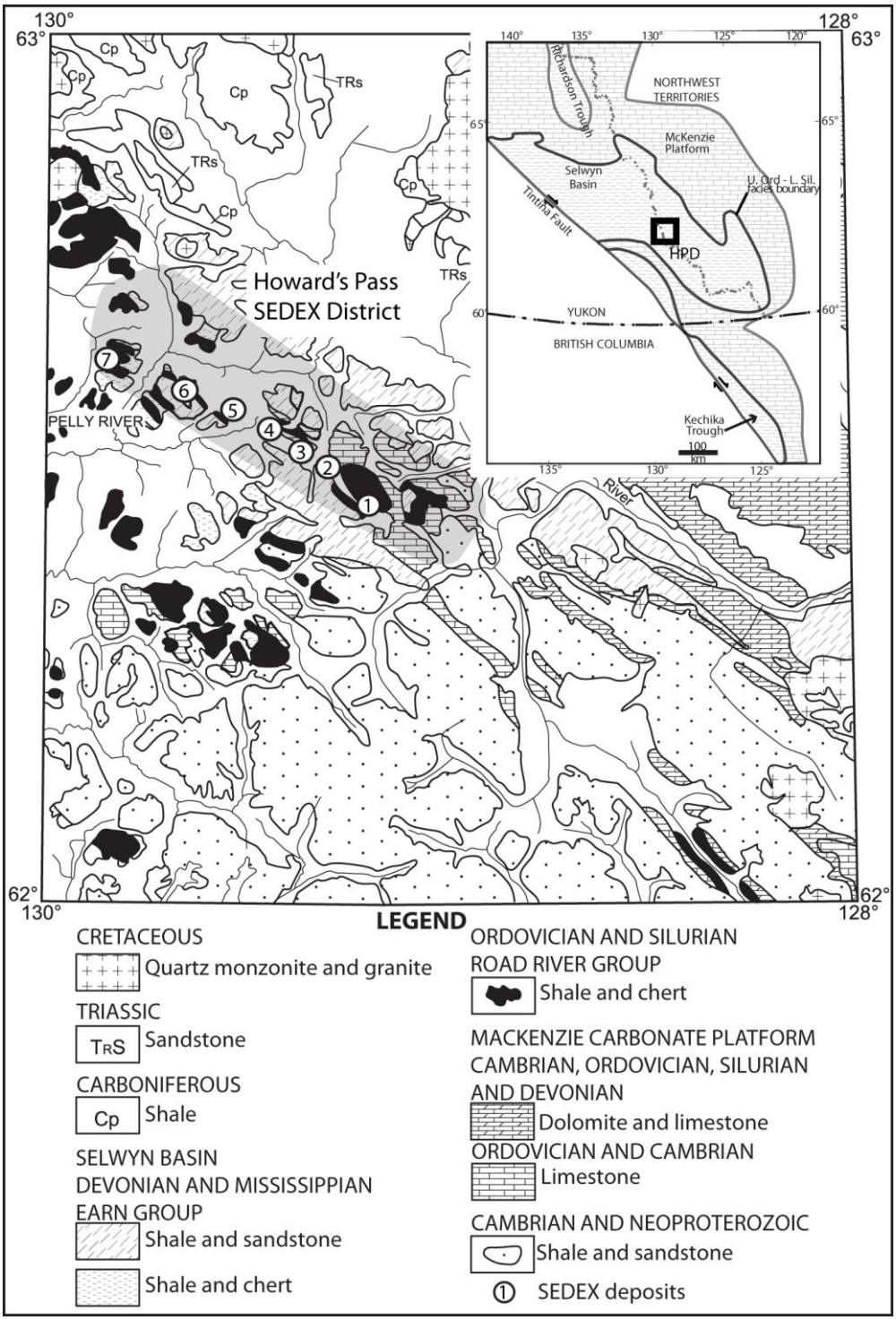

Figure 1: Generalized geologic map of the Howard's Pass district showing locations of SEDEX Zn-Pb deposits and mineralized zones with inset location of Selwyn Basin in the northern Cordillera. 1: XY zone (XY, XY Central and XY West deposits); 2: Brodel deposit; 3: HC zone (HC and HC West deposits); 4: Don zone (Don and Don East deposits); 5: Anniv Zone (Anniv and Anniv East deposits); 6: OP deposit; 7: Pelly North deposit.

We have used standard petrographic reflected light microscopy, together with field emission gun-environmental scanning electron microscopy (FEG-ESEM) and laser ablation-inductively coupled plasma-mass spectrometry (LA-ICP-MS) to determine the minor and trace element compositions of the different textural styles and generations of pyrite in host rocks and in Zn-Pb SEDEX deposits of the HPD. We have also used SIMS to determine the sulphur isotope compositions of these pyrites. The objectives of this study were to apply these *in situ* analytical techniques to differentiate between ore stage pyrite, diagenetic pyrite and metamorphic pyrite. Whereas bulk analysis is insensitive to textural complexity, our *in situ* data reveal that the trace element and sulphur isotope compositions of these various textural types and stages of pyrite reflect precipitation from hydrothermal, hydrogenous, diagenetic and metamorphic fluids.

Results/Data Analysis

Petrography and SIMS sulphur isotopes

The HPD is hosted in sedimentary strata of the Duo Lake Formation. These rocks are dominantly carbonaceous siliceous to calcareous mudstones. Locally, the Duo Lake Formation is subdivided into informal members that, from base to top, comprise the Calcareous Mudstone member (CCMS), Active member (ACTM) and Upper Siliceous Mudstone member (USMS) (Morganti, 1979). The Steel Formation conformably overlies the Duo Lake Formation and is locally named the Flaggy Mudstone member (FLMD) (Morganti, 1979). The ACTM hosts the major SEDEX Zn-Pb deposits in the HPD. Conodont age dating by Norford and Orchard (1985) reveals that the ACTM was deposited in the Early Silurian (~440 Ma). These authors also show that the ACTM is stratigraphically bracketed between two graptolite zones that restrict deposition to a maximum of 5 m.y. Pyrite is a minor but ubiquitous component of these sedimentary rocks and constitutes approximately 4.6 wt.% of the CCMS, 5.4 wt.% of the ACTM and 2.9 wt.% of the USMS (Gadd et al., unpublished data).

Reflected light microscopy reveals multiple generations of pyrite growth in the succession of sedimentary rocks of the HPD. Pyrite occurs as framboids, polyframboidal clusters (Figure 2A) and micro-euhedra, bedding parallel bands (Figure 2B), nodules (Figure 2C), and porphyroblasts and metamorphic overgrowths (Figure 2D). Pyrite framboids and minute euhedra (py1) consist of spherical aggregates of micro-crystalline pyrite and irregular aggregates of minute pyrite crystals, respectively. Individual framboids are generally <10 μm to 20 μm in diameter, and less commonly up to 50 μm in diameter. Framboidal py1 occurs locally as agglomerated masses of several hundred microns across, which form polyframboids. Minute (1-5 μm diameter) py1 euhedra occur as crystals in irregular masses. Although framboidal py1 occurs in the Duo Lake and Steel formations, it is most abundant in the upper portion of the ACTM, forming delicate laminae intercalated with carbonaceous sediments, sphalerite and galena. The sulphur isotope composition of py1 from the ACTM of the XY Central, Don, Don East and Anniv East deposits has negative $\delta^{34}S$ values that

range from -26.1 to -7.5‰ (Figure 3). Framboids from the USMS also display negative $\delta^{34}S$ values (-21.0 to -15.7‰).

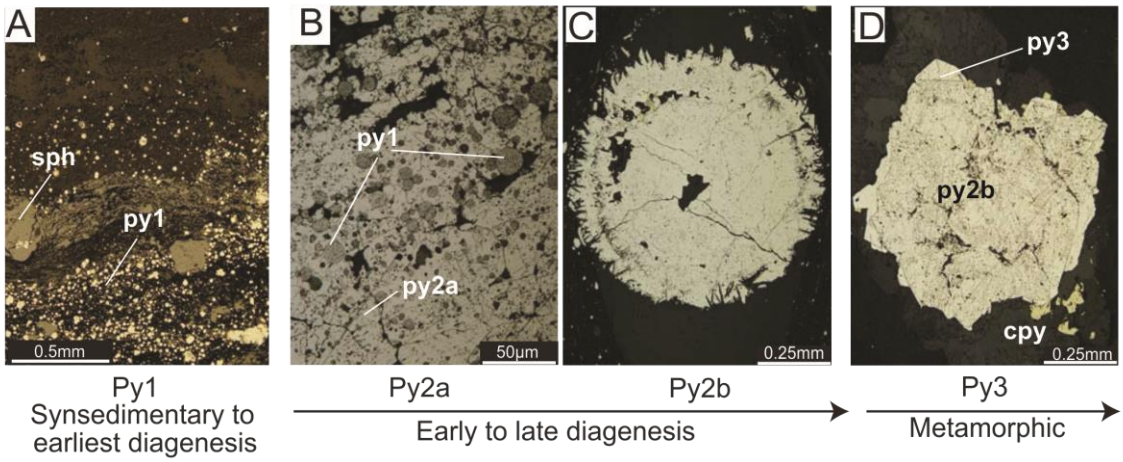

Figure 2: Pyrite paragenesis shown by representative photomicrographs of pyrite generations and textures. Abbreviations: py=pyrite; sph=sphalerite; cpy=chalcopyrite.

Bedding-parallel pyrite layers <1 mm to several mm thick (py2a) occur as wispy laminae of aggregated and intergrown subhedral to euhedral crystals (Figure 2B). Py2a forms wispy and discontinuous layers to well-formed continuous beds at the drill core scale. Py2a is common within the CCMS, ACTM and USMS, but is rare in the FLMD. Well-formed py2a layers overprint and preserve primary bedding of the host carbonaceous mudstones. Wispy py2a differs from laminated py1 in that the framboidal texture is either overprinted (Figure 2B) or obliterated due to post-depositional recrystallization. Pyrite nodules (py2b) comprise round to sub-round masses of intergrown and aggregated subhedral pyrite crystals that commonly show radial growth patterns and herringbone textures (Figure 2C). Nodules range in diameter from 0.5 to >1.5 cm and occur throughout the stratigraphic succession. Py2b nodules typically display complex growth textures that range from sooty (silicate inclusion-rich) to clear (inclusion-free). Etching of polished surfaces with concentrated HNO_3 enhanced textures and revealed growth relationships among pyrite generations, such as where py2b overprinted and recrystallized polyframboidal py1.

The diagenetic varieties of bedded (py2a) and nodular pyrite (py2b) are isotopically indistinguishable in a given stratigraphic unit and are, therefore, grouped together in the histograms of Figure 3. Diagenetic pyrites have exclusively positive sulphur isotope values. Within the CCMS ($\delta^{34}S$ +13.4 to 47.8‰), ACTM ($\delta^{34}S$ +21.9 to 47.7‰) and USMS ($\delta^{34}S$ +14.7 to 49.7‰), this type of pyrite contains broadly similar ranges of values. Within the FLMD, the $\delta^{34}S$ values have a slightly narrower range that is lower than for pyrite from the Duo Lake Formation ($\delta^{34}S$ +10.3 to 35.7‰). Samples that have diagenetic pyrite overgrowing framboidal pyrite, or diagenetic pyrite and framboidal pyrite coexisting, display more complex sulphur isotope systematics. In places, the heavy positive $\delta^{34}S$ values of diagenetic pyrite are juxtaposed by light negative values of framboids, resulting in $\Delta^{34}S_{py2\text{-}py1}$ of 40‰ over distances of <50 µm.

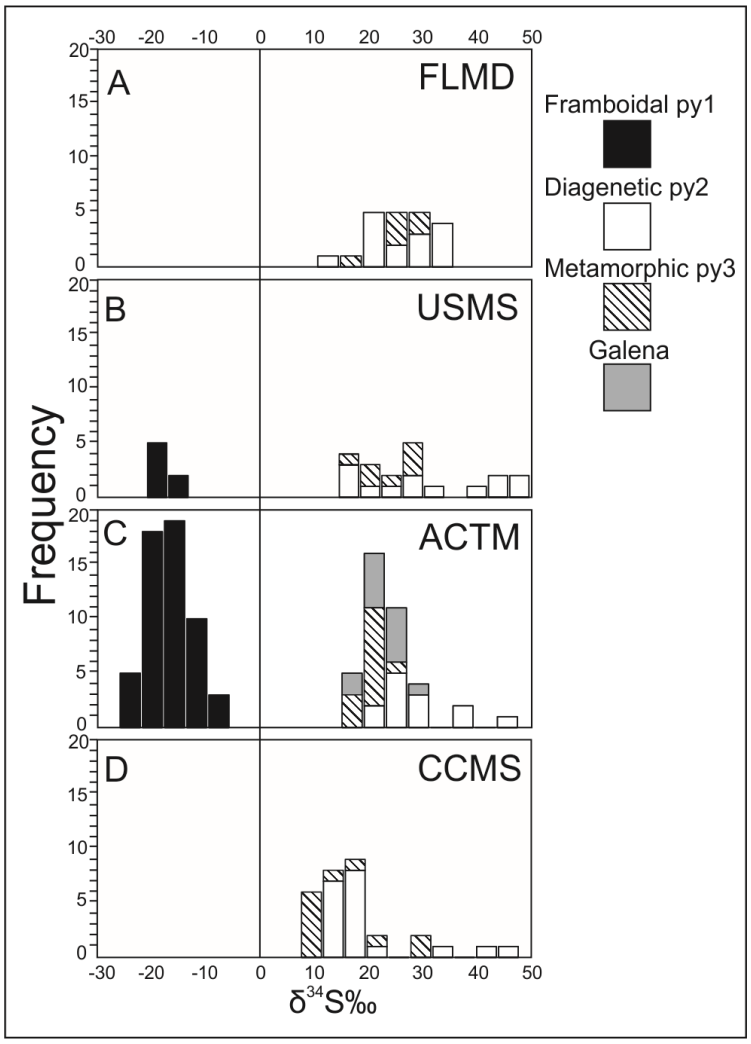

Figure 3: Histograms of SIMS sulphur isotope compositions of individual pyrite generations and galena from A) FLMD, B) USMS, C) ACTM and D) CCMS units.

Metamorphic pyrite (py3) occurs as both euhedral crystals and thin (<0.2 mm) overgrowths on pre-existing pyrites. Py3 is the latest stage of pyrite growth in the HPD and overgrows all preceding generations. Euhedral py3 crystals are between 0.1 and 50 mm in diameter and are crystallographically aligned with the regional cleavage. Metamorphic overgrowths of py3 form veneers on diagenetic pyrites (Figure 2D). The sulphur isotope values of py3 are also positive, but are generally lower than those of diagenetic pyrite. The $\delta^{34}S$ values of py3 range from moderately to highly positive (+7.5 to +30.4‰). Veneers of py3 on diagenetic pyrite are lighter than the diagenetic pyrite on which the veneers form, but the difference in $\delta^{34}S$ values (1 to 20‰) is not as pronounced as that between py1 and py2.

Sphalerite and galena occur together with pyrite throughout the Duo Lake Formation and are concentrated within the ACTM. Inclusions of sphalerite and

galena in pyrite are generally small (<0.2 mm) and form fracture fillings within, and interstitial to, adjacent pyrite crystals. Sulphur isotope compositions of galena were determined for two samples (total of 13 spot analyses), for galena that shares grain boundaries with both framboidal and euhedral diagenetic-metamorphic pyrite. The $\delta^{34}S$ values of galena are highly positive (+17.0 to +27.3‰) and are, on average, 39.0‰ heavier than the framboids. Galena and adjacent diagenetic-metamorphic pyrite display nearly identical average sulphur isotope compositions; however, the average $\delta^{34}S$ value of diagenetic pyrite in the ACTM is 7‰ heavier than that of galena. Sphalerite was not analyzed using SIMS; however, the bulk $\delta^{34}S$ value of sphalerite in the HPD is moderately to highly positive (+12.6 to +23.3‰) (I.R. Jonasson, pers. comm., 2014).

LA-ICP-MS

The minor and trace element compositions of py1 (*n* = 114), py2a (*n* = 144), py2b (*n* = 229), and py3 (*n* = 112) were determined by LA-ICP-MS. A series of parallel and adjacent line rasters across pyrite crystals measured the distributions and contents of minor and trace elements. Pyrite within the HPD contains a broad suite of trace elements, the most abundant of which are Mn, Co, Ni, Cu, Zn, As, Se, Ag, Sb, Tl, and Pb. The contents of these elements vary among pyrite generations and the stratigraphic position of the host rocks in which they reside. Trace element variability in pyrite that displays multiple growth zones is coincident with textural and morphological variability (Figure 4).

All of these elements occur in variable quantities. However, pyrite is not the exclusive host of Zn, Pb, Cu, and Mn. Minute inclusions of sphalerite (Zn), galena (Pb), and chalcopyrite (Cu) are common within pyrite; LA-ICP-MS reveals that the highest contents of these elements are associated with such mineral inclusions. Calcite sequesters some Mn, but it also occurs in pyrite. The other trace elements present (Co, Ni, As, Se, Ag, Sb, and Tl) are predominantly hosted in pyrite. Within the ACTM, however, Se and Ag are mainly sequestered in galena.

Discussion/Models

Pyrite formation and timing of SEDEX mineralization

Goodfellow (2004) suggested that mineralizing fluids responsible for the HPD SEDEX deposits were dense, bottom-hugging brines that exhaled from a submarine vent distal to the deposits, in pulses related to the reactivation of early growth faults. In this model, the brine migrated to, and eventually settled into, a bathymetric low (i.e. the Howard's Pass sub-basin), and sphalerite, galena and framboidal pyrite are products of chemical sedimentation in a density- and redox-stratified water column.

The model of Goodfellow (2004) also stipulates that the water column is the primary reservoir of reduced sulphur, where bacterial sulphate reduction (BSR) consumed a diminishing quantity of sulphate. Goodfellow (1987) proposed that the effects of BSR and Rayleigh fractionation are recorded in the sulphur isotope

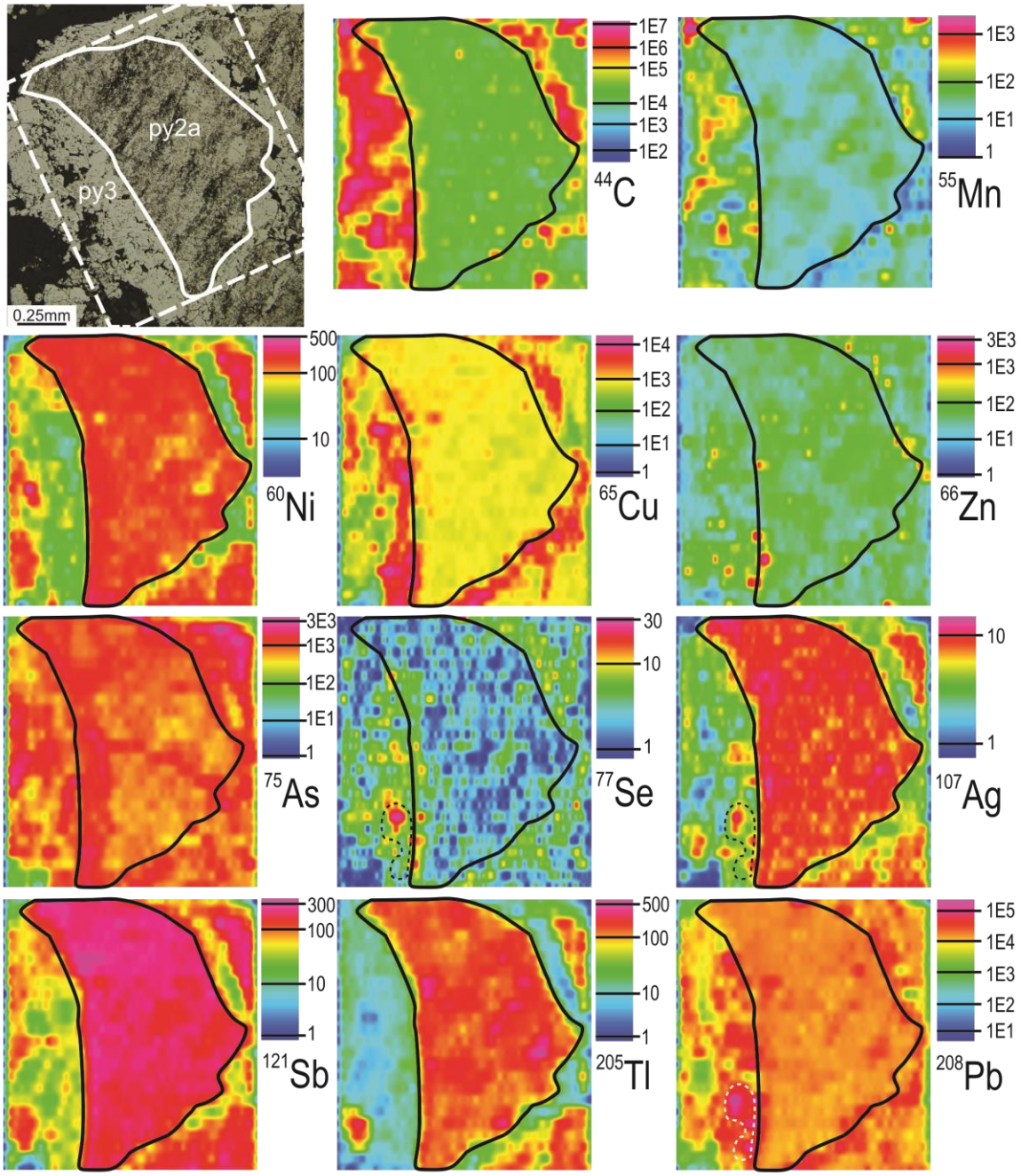

Figure 4: Photomicrograph (upper left) accompanying trace element distribution maps of py2a-py3 in ACTM sample Don-200-382.0. Framboidal py1, if present, has been pervasively recrystallized such that primary textures are obliterated. Colour ramps are shown in linear ppm except for Ca, which is in counts per second.

compositions of sedimentary pyrite, which become progressively heavier stratigraphically upward from the CCMS to the USMS (Figure 5). Whereas the SIMS data for diagenetic pyrite yield similar $\delta^{34}S$ values to those previously reported for pyrite in the HPD (Goodfellow, 1987), the sulphur isotope compositions of pyrite framboids are strikingly different (Figures 3C, 5). From a paragenetic standpoint, framboidal py1 is the earliest generation to form and it is likely that growth of this pyrite occurred either in an euxinic water near the sediment-water interface or in the uppermost sulphidic sediment porewaters of unconsolidated sediments. The $\delta^{34}S$ values of framboids, therefore, should provide the most reliable estimate of the sulphur isotope composition of ambient reduced sulphur (e.g. Lyons, 1997). If a kinetic fractionation of 45‰ is assumed between bacterially reduced parent sulphate and daughter sulphide (Sweeney and Kaplan, 1980; Strauss, 1999), then the $\delta^{34}S$ values of framboids in the SEDEX deposits of the HPD are consistent with derivation of sulphide from unfractionated coeval seawater sulphate (~28‰; Claypool et al., 1980; Kampschulte and Strauss, 2004). Significantly, $\delta^{34}S$ values of sphalerite (I.R. Jonasson, pers. comm., 2014) and galena (this study) are much heavier than those of framboidal pyrite. By inference, therefore, the base metal sulphides and framboids lack a common source of sulphur or are not coeval (see Ohmoto and Goldhaber, 1997).

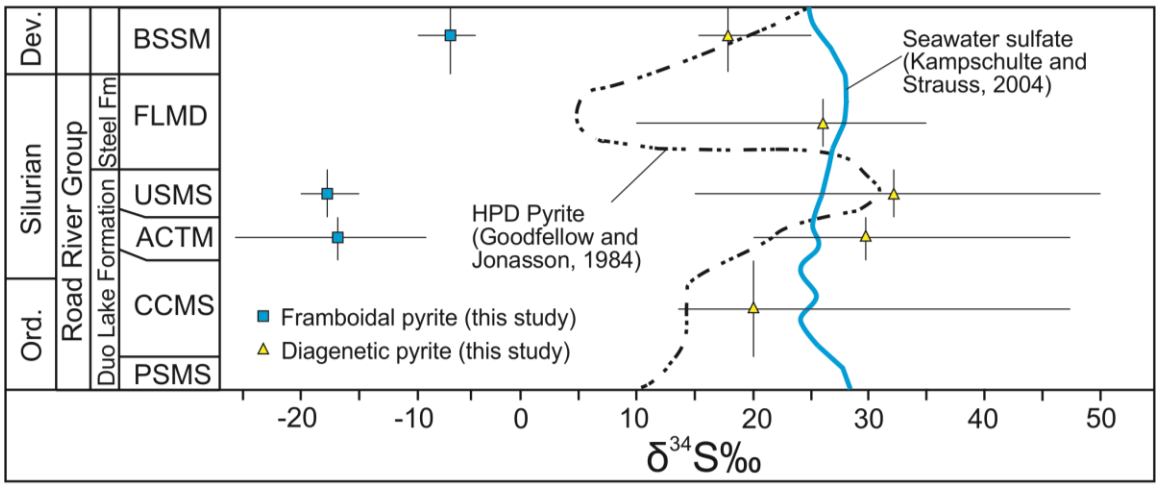

Figure 5: Secular distribution of $\delta^{34}S$ values for sedimentary pyrite (Goodfellow and Jonasson, 1984) and seawater sulphate (Kampschulte and Strauss, 2004) together with SIMS $\delta^{34}S$ values of framboidal and diagenetic pyrite. Note similarities between $\delta^{34}S$ values of diagenetic pyrite determined in this study and those of sedimentary pyrite reported by Goodfellow and Jonasson (1984). The $\delta^{34}S$ values of diagenetic pyrite is consistently heavier than those of framboidal pyrite (modified after Goodfellow and Jonasson, 1984).

Pyrite is a fairly refractory mineral and can retain its primary trace element and sulphur isotope compositions during low-grade metamorphism, but pervasive recrystallization in the presence of hydrothermal fluids can alter its primary composition (Williford et al., 2011; Large et al., 2014). Framboidal py1 contains relatively high contents of hydrothermal elements such as Tl, As, Mn and Sb. The

highest contents of these elements in the ACTM, however, are generally within py2a and py2b that have nearly obliterated py1 (Figure 4). Preferential incorporation of such hydrothermal elements into py2a and py2b indicates that diagenetic pyrite in the ACTM formed during the Zn-Pb ore-stage. Py2a and py2b postdate py1, implying that the SEDEX mineralization postdates formation of the framboidal pyrite.

Hydrothermal fluid properties and transport

Sangster (2002) experimentally modelled the transport of dense brine into sedimentary basins and showed that the brines could travel relatively far from the source area. These experiments used sand as the sediment medium as opposed to fine-grained mud; lithified equivalents of the latter (mudstone, shale, slate) typically host SEDEX Zn-Pb (±Ba ±Ag) deposits. Mud is much less permeable than sand, but has high initial porosity that is retained for tens to hundreds of meters below the sediment-water interface (Einsele, 2000). Warm basinal brines are capable of carrying significant concentrations of dissolved metals (Hanor, 1979; Sangster, 2002; Yang et al., 2004). A consequence of the density contrast between the brines and sediment porewaters is the displacement of less dense sediment porewaters into the basin margins and into the overlying water column (Sangster, 2002). The products of this fluid exchange would be pyrite enriched in the trace elements of the dense brine, and depleted in those of the porewaters. Assuming that SEDEX fluid contained hydrothermal elements (Zn, Pb, Ag, Tl, As, Sb ± Mn) and was deficient in other elements (e.g. Co, Ni, Cu, Se, etc.), then this process could explain the different distributions of trace elements among pyrite types contained within the ACTM (Gadd et al., in review).

Unlike other SEDEX Zn-Pb districts (e.g. MacMillan Pass), a plumbing system has not been recognized within the HPD. Nevertheless, synsedimentary faults were likely the conduit for fluid delivery. Our data indicate that the mineralizing process was more complex than proposed by previous workers, and that framboidal pyrite was not a hydrothermal product; rather, framboids are solely of synsedimentary to early diagenetic origin. The model we propose involves the ponding of hydrothermal brine in a redox stratified water column, and percolation of this brine into sulphidic, unconsolidated carbonaceous muds (Figure 6A). Dense sinking brine forced sulphidic porewaters out of muddy sediments, resulting in hydrothermal chemical sedimentation in the lower brine pool where particulate galena, sphalerite and pyrite accumulated on the basin floor. As dense brine sank into muds, porewater sulphate was reduced by the oxidation of labile organic matter. *In situ* carbon dioxide generation and coeval base metal sulphide precipitation resulted in CO_2 build-up within partially cemented fine-grained muds. The loss of permeability by sulphide precipitation coupled with increased pCO_2 generated over-pressurized pore fluids and eventually resulted in upward migration of pore fluids. These features are preserved in the HPD as ‘dewatering pipes’ (e.g. Jonasson and Goodfellow, 1986) that cross-cut laminated sediments during diagenesis. Dewatering promoted further mixing at the brine-seafloor interface (Figure 6B).

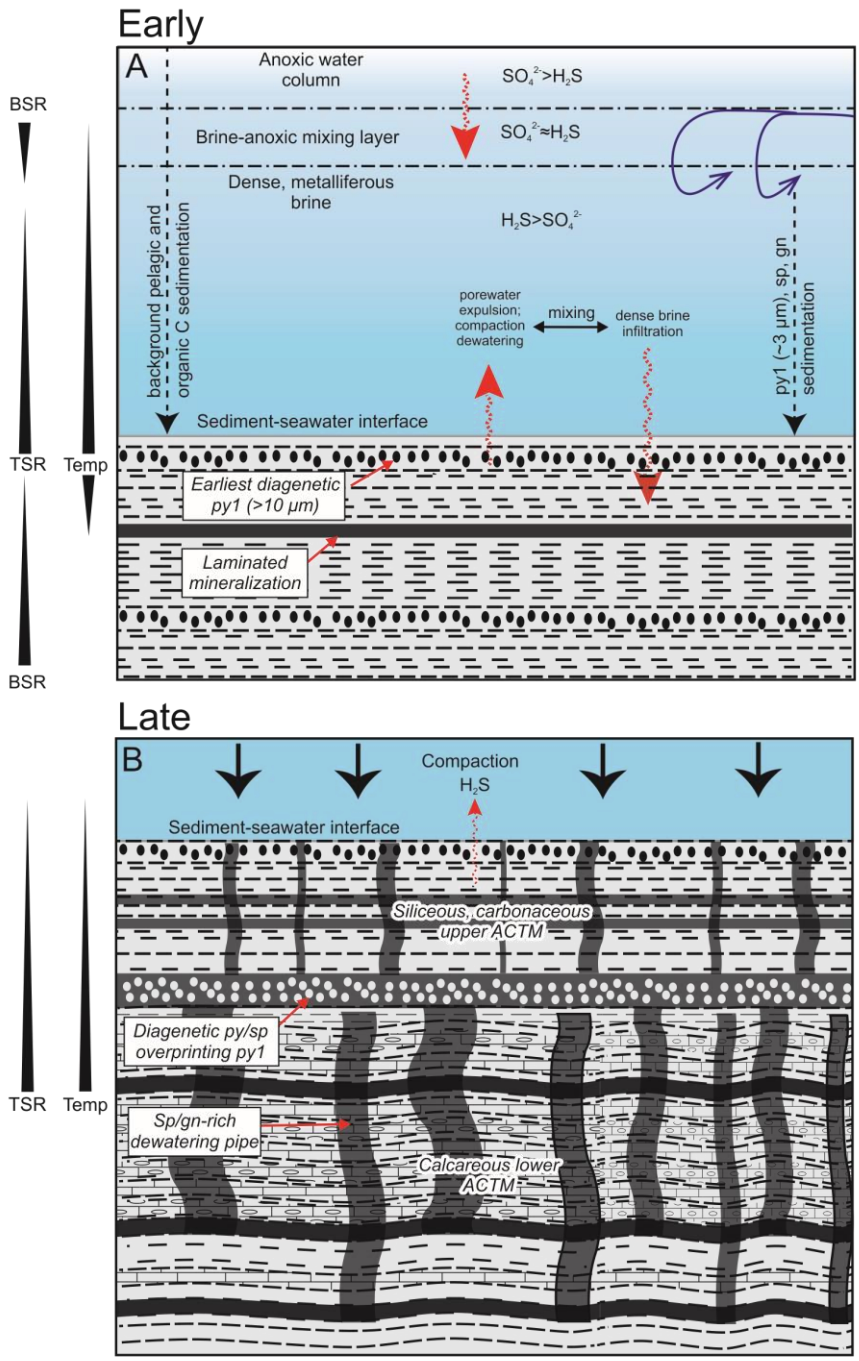

Figure 6: Schematic model for formation of SEDEX Zn-Pb deposits in HPD. The model accounts for SIMS sulphur isotope data and illustrates controls on sulphate-sulphide distribution and sulphate reducing processes. A) Synsedimentary sulphide deposition is accompanied by sinking of dense brine into permeable muds, where metals and sulphate are transported together. Dense brine sinking displaces less-dense sulphidic porewaters and promotes early TSR; B) sinking brines percolate into muds and precipitate diagenetic sulphides that form overgrowths on pre-existing sulphides and calcite intercalated with carbonaceous sediments. Loss of permeability is likely followed by compaction and dewatering, which promotes mixing at the sediment-water interface (no scale implied; adapted and modified from Ireland et al., 2004).

The SIMS sulphur isotope data support this model of SEDEX mineralization in the HPD. Limited permeability of fine-grained argillaceous sediments precludes deep (>100s m) brine percolation of brines (Einsele, 2000); however, in the HPD it is unlikely that mineral deposition occurred entirely in the water column because complex sulphur isotope systematics do not support a purely synsedimentary origin for the formation of SEDEX Zn-Pb deposits (cf., Goodfellow, 1987). Isotopically heavy $\delta^{34}S$ values for galena and diagenetic pyrite mantle framboids having very low values, suggesting that deposition of galena and py2 followed that of py1 in the ACTM. Goodfellow (1987) indicated that the reduced sulphur in the mineral deposits was entirely derived from an anoxic water column, but this model is difficult to reconcile with the discrepancy in the global secular curve for sulphur isotopic compositions of seawater sulphate and our data for sulphides (Figure 5). We propose that additional (oxidized) sulphur was delivered with base metals to an ambient euxinic water column and that both BSR and thermochemical sulphate reduction (TSR) generated reduced sulphur in the HPD SEDEX deposits (Figure 6). BSR was the most important process prior to the introduction of metalliferous hydrothermal fluids that provided a necessary catalyst for TSR. TSR superseded BSR following the introduction of metalliferous fluids because these fluids were too warm (>100°C) to support significant bacterial activity. In the early stage of hydrothermal activity, TSR was likely restricted to the lowermost water column, near the sediment-water interface (Figure 6A). Continued venting of dense brine resulted in its downward percolation into porous unconsolidated muds, where TSR reduced hydrothermally derived sulphate by the oxidation of labile organic carbon (Figure 6B).

Calcite, the most abundant carbonate mineral in the HPD, is a major component of the ACTM and is characterized by isotopically light $\delta^{13}C$ values (typically -3 to -6‰) (I.R. Jonasson, pers. comm., 2014). The calcite content of the ACTM is variable, and some of the highest calcite abundances occur immediately above sections of semi-massive to massive sphalerite and galena mineralization (Gadd et al., unpublished data). It should be noted that portions of the ACTM are predominantly calcareous without underlying sulphides. Importantly, the isotopically light $\delta^{13}C$ values for ACTM fall within a range consistent with those typically produced by TSR, whereas much lower $\delta^{13}C$ values would be expected for significant BSR or anaerobic methane oxidation calcite (Machel, 2001).

A similar model has been presented for the HYC Zn-Pb-Ag SEDEX deposit in northern Australia (Ireland et al., 2004). On the basis of mineral textures and sulphur isotope compositions, these authors proposed that synsedimentary and syndiagenetic mineralization are products of complex interactions among metalliferous brines, reduced porewaters and reduced bottom waters. These similarities suggest that the HPD (and perhaps other SEDEX deposits within the Selwyn Basin) and Australian SEDEX deposits have more in common than was recognized previously (Cooke et al., 2000). The dense, sinking brine pool model is not without shortcomings, however. Namely, the absence of empirical salinity

and temperature data for the SEDEX mineralizing fluids imposes limitations on a brine pool model. Mound structures and footwall feeder zones also have not been identified in the HPD. Nonetheless, trace element and sulphur isotope variations between pyrite generations and the enrichment of SEDEX-associated elements in diagenetic pyrite reported here support this sinking brine pool model of Zn-Pb mineralization in the HPD.

Implications for Exploration

LA-ICP-MS analyses reveal strong textural control on the distribution of trace elements in pyrite from a variety of settings. This methodology is costly and time consuming, and it is unlikely that it will be widely adopted by industry; however, our data reveal that careful selection of pyrite for analysis can yield valuable information about the hydrothermal processes involved in SEDEX formation. Pyrite chosen for analysis should be sooty (i.e. inclusion-rich) and composed of fine-grained aggregates. Bedded (laminated) and nodular pyrite are both suitable, whereas coarse euhedral metamorphic pyrite is not. Large nodules (>2 cm) are suitable for trace element analysis. The interior, paragenetically earlier regions of nodular pyrite are more likely to contain higher contents of trace elements than the exterior, later regions. Etching flat pyrite surfaces with concentrated nitric acid can enhance textural variability and improve sample selection.

Pyrite sequesters several trace elements in the HPD, of which Tl, As, Sb and possibly Mn are considered hydrothermal in origin. Ore-stage diagenetic pyrite contains, on average, >50 ppm Tl, >800 ppm As, >70 ppm Sb and >500 ppm Mn. These abundances are not significantly higher than those of average Paleozoic diagenetic pyrite (Large et al., 2014), nor are they as high as the abundances that characterize other SEDEX deposits (e.g. Red Dog, Alaska; Graham et al., 2009); however, they are high in the HPD where associated with SEDEX Zn-Pb mineralization. The common occurrence of minute grains of sphalerite and galena within pyrite indicates that these elements should also be analyzed. For bulk analysis of pyrite separates, the recommended method of digestion is using aqua regia, because it dissolves sulphide minerals without also dissolving most silicates, thus effectively avoiding dilution by these less-soluble minerals.

Several Paleozoic SEDEX Zn-Pb districts in the Yukon and northeast British Columbia contain significant barite units that are genetically linked to SEDEX mineralization. Significantly, however, barite is absent within the SEDEX Zn-Pb deposits of the HPD. The Ba content of the ACTM, <1000 ppm, is much lower than that of the underlying and overlying sedimentary rocks of the Duo Lake Formation. Positive correlations between Ba, Al and K suggest that the Ba present in the ACTM occurs as hyalophane (Ba-feldspar) and not barite (see also Goodfellow and Jonasson, 1986). Barite is present in the FLMD, but this unit postdates mineralization by several million years, and hence it is unlikely that this barite is genetically related to the underlying SEDEX Zn-Pb mineralization. Therefore, exploration for SEDEX deposits similar those known in the HPD should not expect to find significant quantities of barite.

Future Work

The succession of rocks that host SEDEX deposits in the HPD is variably phosphatic, and the sedimentary rocks immediately above these deposits (USMS) contain up to 10 wt% P_2O_5. Previous studies in the 1980s interpreted this unit as being the product of metal-poor, phosphorus-rich hydrothermal venting. However, the body of research on sedimentary phosphorite deposition has grown considerably since these early studies. Preliminary studies by scientists from the U.S. Geological Survey have shown that phosphogenesis in the HPD is likely related to nutrient-rich upwelling, and is not the product of hydrothermal venting. This research will likely provide insights into the geochemically complex depositional and diagenetic environments of the HPD. Implications of this research could potentially redefine the depositional environment of the HPD, allowing the use of better-tailored exploration models for this genetically enigmatic seafloor-hydrothermal system.

The data we present here is exclusively on rocks that are proximal to the SEDEX mineralization (i.e, directly overlying and underlying the deposits). Sampling of unweathered, age-equivalent carbonaceous mudstone distal to mineralization should be undertaken to properly evaluate the presence and/or extent of widespread hydrothermal alteration of the host rocks in the region.

Acknowledgements

This research was jointly funded by TGI-4 of the Geological Survey of Canada, NSERC-DG and CAMIRO Project 08E04 “Geochemistry of Shales as Vectors to Ore Deposits”. We thank Jason Dunning, Gabe Xue, Wolfgang Schleiss and Jelle de Bruyckere of Selwyn Chihong Mining Ltd. for providing access to drill cores and technical information, without which this work could not have been done. We also thank the Society of Economic Geologists Canada Foundation for financial support.

References

Berner, R.A., 1984, Sedimentary pyrite formation: An update: Geochimica et Cosmochimica Acta, v. 48, p. 605-615.

Berner, Z., Puchelt, H., Nölt er, T., and Kramar, U., 2013, Pyrite geochemistry in the Toarcian Posidonia Shale of south-west Germany: Evidence for contrasting trace-element patterns of diagenetic and syngenetic pyrites: Sedimentology, v. 60, p. 548-573.

Claypool, G.E., Holser, W.T., Kaplan, I.R., Sakai, H., and Zak, I., 1980, The age curves of sulfur and oxygen isotopes in marine sulfate and their mutual interpretation: Chemical Geology, v. 28, p. 199-260.

Cooke, D.R., Bull, S.W., Large, R.R., and McGoldrick, P.J., 2000, The importance of oxidized brines for the formation of Australian Proterozoic stratiform sediment-hosted Pb-Zn (Sedex) deposits: Economic Geology, v. 95, p. 1-18.

Einsele, G., 2000, Sedimentary basins: Evolution, facies, and sediment budget:

Berlin Heidelberg, Springer, 792 p.
Eldridge, C.S., Compston, W., Williams, I.S., Both, R.A., Walshe, J.L., and Ohmoto, H., 1988, Sulfur isotope variability in sediment-hosted massive sulfide deposits as determined using the ion microprobe SHRIMP: I, An example from the Rammelsberg orebody: Economic Geology, v. 83, p. 443-449.
Eldridge, C.S., Williams, N., and Walshe, J.L., 1993, Sulfur isotope variability in sediment-hosted massive sulfide deposits as determined using the ion microprobe SHRIMP: II, A study of the H.Y.C. deposit at McArthur River, Northern Territory, Australia: Economic Geology, v. 88, p. 1-26.
Goodfellow, W.D., 1987, Anoxic stratified oceans as a source of sulphur in sediment-hosted stratiform Zn-Pb deposits (Selwyn Basin, Yukon, Canada): Chemical Geology: Isotope Geoscience Section, v. 65, p. 359-382.
Goodfellow, W.D., 2004, Geology, genesis, and exploration of SEDEX deposits, with emphasis on the Selwyn Basin, Canada, *in* Deb, M., and Goodfellow, W.D., ed., Sediment-hosted lead-zinc sulphide deposits: Attributes and models of some major deposits of India, Australia, and Canada: Delhi, India, Narosa Publishing House, p. 24–99.
Goodfellow, W.D., and Jonasson, I., 1986, Environment of formation of the Howards Pass (XY) Zn-Pb deposit, Selwyn Basin, Yukon, *in* Morin, J.A., ed., Mineral deposits of northern Cordillera: Canadian Institute of Mining and Metallurgy, special volume 37, p. 19-50.
Goodfellow, W.D., and Jonasson, I.R., 1984, Ocean stagnation and ventilation defined by $\delta^{34}S$ secular trends in pyrite and barite, Selwyn Basin, Yukon: Geology, v. 12, p. 583-586.
Goodfellow, W.D., Jonasson, I.R., and Morganti, J.M., 1983, Zonation of chalcophile elements about the Howard's Pass (XY) Zn-Pb deposit, Selwyn Basin, Yukon: Journal of Geochemical Exploration, v. 19, p. 503-542.
Graham, G.E., Kelley, K.D., Slack, J.F., and Koenig, A.E., 2009, Trace elements in Zn-Pb-Ag deposits and related stream sediments, Brooks Range Alaska, with implications for Tl as a pathfinder element: Geochemistry: Exploration, Environment, Analysis, v. 9, p. 19-37.
Gregory, D., Meffre, S., and Large, R., 2014, Comparison of metal enrichment in pyrite framboids from a metal-enriched and metal-poor estuary: American Mineralogist, v. 99, p. 633-644.
Hanor, J.S., 1979, Sedimentary genesis of hydrothermal fluids, *in* Barnes, H. L., ed., Geochemistry of hydrothermal ore deposits: New York, John Wiley and Sons, p. 137-168.
Ireland, T., Large, R.R., McGoldrick, P., and Blake, M., 2004, Spatial distribution patterns of sulfur isotopes, nodular carbonate, and ore textures in the McArthur River (HYC) Zn-Pb-Ag deposit, Northern Territory, Australia: Economic Geology, v. 99, p. 1687-1709.
Jonasson, I.R., and Goodfellow, W.D., 1986, Sedimentary and diagenetic textures, and deformation structures within the sulphide zone of the Howards Pass (XY) Zn-Pb deposit, Yukon and Northwest Territories, *in* Morin, J. A., ed., Mineral deposits of northern Cordillera: Canadian Institute of Mining and Metallurgy, special volume 37, p. 51-70.

Kampschulte, A., and Strauss, H., 2004, The sulfur isotopic evolution of Phanerozoic seawater based on the analysis of structurally substituted sulfate in carbonates: Chemical Geology, v. 204, p. 255-286.
Large, R.R., Danyushevsky, L., Hollit, C., Maslennikov, V., Meffre, S., Gilbert, S., Bull, S., Scott, R., Emsbo, P., Thomas, H., Singh, B., and Foster, J., 2009, Gold and trace element zonation in pyrite using a laser imaging technique: Implications for the timing of gold in orogenic and Carlin-style sediment-hosted deposits: Economic Geology, v. 104, p. 635-668.
Large, R.R., Halpin, J.A., Danyushevsky, L.V., Maslennikov, V.V., Bull, S.W., Long, J. A., Gregory, D.D., Lounejeva, E., Lyons, T.W., Sack, P.J., McGoldrick, P.J., and Calver, C.R., 2014, Trace element content of sedimentary pyrite as a new proxy for deep-time ocean–atmosphere evolution: Earth and Planetary Science Letters, v. 389, p. 209-220.
Lyons, T.W., 1997, Sulfur isotopic trends and pathways of iron sulfide formation in upper Holocene sediments of the anoxic Black Sea: Geochimica et Cosmochimica Acta, v. 61, p. 3367-3382.
Machel, H.G., 2001, Bacterial and thermochemical sulfate reduction in diagenetic settings—old and new insights: Sedimentary Geology, v. 140, p. 143-175.
Morganti, J.M., 1979, The geology and ore deposits of the Howards Pass Area, Yukon and Northwest Territories: the origin of basinal sedimentary stratiform sulphides deposits: unpublished PhD thesis, University of British Columbia, 351 p.
Norford, B.S., and Orchard, M.J., 1985, Early Silurian age of rocks hosting lead-zinc mineralization at Howards Pass, Yukon Territory and District of Mackenzie: Geological Survey of Canada Paper 83-18, 35 p.
Ohmoto, H., and Goldhaber, M.B., 1997, Sulfur and carbon isotopes, *in* Barnes, H.L., ed., Geochemistry of hydrothermal ore deposits: New York, John Wiley and Sons, p. 517-611.
Raiswell, R., and Berner, R.A., 1985, Pyrite formation in euxinic and semi-euxinic sediments: American Journal of Science, v. 285, p. 710-724.
Sangster, D., 2002, The role of dense brines in the formation of vent-distal sedimentary-exhalative (SEDEX) lead-zinc deposits: Field and laboratory evidence: Mineralium Deposita, v. 37, p. 149-157.
SCML, 2012, Selwyn announces updated mineral resource for XY West deposit: Vancouver, British Columbia, Canada, p. 1-5.
Strauss, H., 1999, Geological evolution from isotope proxy signals — sulfur: Chemical Geology, v. 161, p. 89-101.
Sweeney, R., and Kaplan, I., 1980, Stable isotope composition of dissolved sulfate and hydrogen sulfide in the Black Sea: Marine Chemistry, v. 9, p. 145-152.
Taylor, B.E., 2004, Biogenic and thermogenic sulfate reduction in the Sullivan Pb–Zn–Ag deposit, British Columbia (Canada): Evidence from micro-isotopic analysis of carbonate and sulfide in bedded ores: Chemical Geology, v. 204, p. 215-236.
Williford, K.H., Van Kranendonk, M.J., Ushikubo, T., Kozdon, R., and Valley, J. W., 2011, Constraining atmospheric oxygen and seawater sulfate

concentrations during Paleoproterozoic glaciation: In situ sulfur three-isotope microanalysis of pyrite from the Turee Creek Group, Western Australia: Geochimica et Cosmochimica Acta, v. 75, p. 5686-5705.

Yang, J., Bull, S., and Large, R., 2004, Numerical investigation of salinity in controlling ore-forming fluid transport in sedimentary basins: Example of the HYC deposit, northern Australia: Mineralium Deposita, v. 39, p. 622-631.